Optimizing the spin Hall effect in Pt-based binary alloys

Oliver L. W. McHugh,[1] Martin Gradhand,[1,2] and Derek A. Stewart[3,*]
[1]*H. H. Wills Physics Laboratory, University of Bristol, Bristol BS8 1TL, United Kingdom*
[2]*Johannes Gutenberg Universität Mainz, Institut für Physik, Staudingerweg 7, 55128 Mainz, Germany*
[3]*Western Digital Research Center, San Jose, California 10005, USA*

(Received 1 October 2023; accepted 15 December 2023; published 18 January 2024)

We present multicode calculations for the spin Hall effect in binary Pt-based alloys, where we explore the viability of alloying the archetype spin Hall material Pt with a large set of metals [Al, Ag, Au, Cu, Hf (hcp), Hf (fcc), Ir, Pd] in order to optimize the charge to spin current conversion for practical applications. To capture intrinsic and extrinsic mechanisms in material-specific calculations, we employ different first-principles codes based on density functional theory in the framework of Green's-function-based multiple scattering approaches. Capturing the transport properties within the relativistic and fully quantum mechanical Kubo-Bastin formalism as well as the semiclassical Boltzmann approach allows for a better understanding of the microscopic physics as well as a larger set of reliable data for the key transport parameters. If available, we compare our results to experimental data, where we generally find good agreement. As we access the full concentration range, we are able to identify the optimal doping regime, which will depend on the binary alloy but generally falls within a region of 60–90 at.% of Pt. When including the unavoidable experimental residual resistivities, the maximum spin Hall angle that we identified is 13% in $Al_{0.2}Pt_{0.8}$ and $Hf_{0.1}Pt_{0.9}$, which is comparable to the best spin Hall angles experimentally found in good metal systems. The longitudinal resistivities in this regime go beyond 70 μΩ cm, which is compatible with metallic-based magnetic random access memory devices.

DOI: 10.1103/PhysRevMaterials.8.015003

I. INTRODUCTION

Spin Hall effect [1–4] (SHE)-based magnetoresistive random access memory (MRAM) devices are posited as an energy efficient and read/write process-resilient form of information storage [5]. Such devices would require large transverse spin currents to be generated from a relatively small longitudinal charge current by the SHE. Therefore, it is of crucial interest to find metallic materials with a large spin Hall angle (SHA), θ_{SH}, defined as the ratio of generated transverse spin current and the corresponding longitudinal charge current. While this parameter is often used as a figure of merit, only a very few computational methods give access to the equally important longitudinal charge conductivity of a given metallic alloy. However, for practical device integration, this parameter is of equal importance. Following this, alloying a known effective spin Hall material in order to manipulate the longitudinal resistance is commonly used to optimize the SHA and improve device integration.

Theoretically, as well as experimentally, Pt is a well-explored spin Hall material [6–8]. Naturally, there have been a number of experimental investigations to test the viability of Pt binary alloys as potential spin Hall materials as, for example, CuPt [9]. Alloying Pt typically considerably reduces the charge conductivity, while only moderately suppressing the spin-orbit coupling and the spin Hall conductivity, which will effectively enhance the SHA. While there have been several experimental studies [6–21] of a variety of these promising alloys, there exists no comprehensive theoretical study on these alloys, especially not across a wide composition range. Modeling a large number of these Pt-based alloys, we identify broader trends, enabling researchers to more readily pick and choose the right combinations.

We have calculated the charge and spin Hall conductivity for seven [Ag, Al, Au, Cu, Hf(fcc), Hf(hcp), Ir, Pd] different chemically disordered binary Pt-based alloys in order to provide the much needed theoretical data. This enables us to systematically optimize the Pt-based alloys for specific applications.

We start by briefly introducing the methodology in Sec. II, after which we present the numerical results for the eight distinct alloys in Sec. III. In all cases, the various contributions will be extracted and compared to other methods, as well as experimental results. Following that, the focus will be on optimizing the performances of the alloys and exploring the maximum of charge to spin current conversion when incorporating the experimentally found residual resistivity. Any trends that are identified will be finally discussed in the conclusions in Sec. IV.

II. METHODOLOGY

The calculations were predominantly performed within the spin-polarized relativistic Korringa-Kohn-Rostoker (SPR-KKR) [29] framework. As we are solving the Dirac equation, spin-orbit coupling is included at all levels and not only

*derek.stewart@wdc.com

TABLE I. Summary of the lattice parameters a_X as well as the residual resistivity ρ_{res} of the constituent elements for all binary alloys. The residual resistivities are taken from experimental results for sputtered thin-film systems at low temperatures typically used in spin transport experiments.

Element	Al (fcc)	Ag (fcc)	Au (fcc)	Cu (fcc)	Hf (hcp)	Ir (fcc)	Pd (fcc)	Pt (fcc)
a_X (Å)	4.048	4.085	4.078	3.618	3.196	3.839	3.891	3.924
ρ_{res} ($\mu\Omega$ cm)	5.9 [22]	1.2 [23]	2.1 [24]	2.9 [25]	6 [26]	0.22 [27]	7 [23]	12 [28]

as a perturbation. This formalism is based on fully relativistic density functional theory (DFT) that leverages the coherent potential approximation (CPA) [30–32] to describe chemically disordered binary alloys across the full composition range. In order to account for the structural change as we explore the composition range, we used Vegard's rule for all of the face-centered-cubic (fcc) alloys. That is, for an alloy $M_{1-x}Pt_x$, the approximate lattice constant is given by

$$a_{M_{1-x}Pt_x} = (1-x)a_M + xa_{Pt}, \tag{1}$$

where a_{Pt} and a_M are the Pt and element M lattice constants, respectively. For the HfPt system, we did not use this approach as Hf and Pt have distinct crystal structures. Here, we performed calculations for fixed lattice constants considering both hexagonal close-packed (hcp) and fcc crystals. While we still calculated the full concentration range for both structures, it should be noted that each system is only of practical relevance in the dilute or moderately dirty regime with a low concentration of Pt or Hf, respectively. In those limits, the systems should be structurally stable as suggested by experimental results [33]. All lattice constants are summarized in Table I. The self-consistent calculations were performed within the local density approximation (LDA) for the exchange correlation functional in the parametrization by Vosko *et al.* [34] and they include a self-consistent loop for the CPA cycle.

While we fully incorporate the chemical disorder of the alloys, we ignore any structural disorder. This is typically a good approximation for concentrated alloys, but becomes more challenging for comparing dilute alloys to experimental observations. In real systems, structural disorder such as dislocations and lattice faults as well as additional impurities will lead to considerable residual resistivities in the dilute limit. In the ultraclean limit of disordered alloys (alloy concentration <2%), this typically results in a dominance of the structural disorder over the chemical disorder in its effect on the overall resistivity. In order to account for this, we include the residual resistivity as a parameter ρ_{res} as derived from experiments.

The transport calculations are based on the solution of the Kubo-Bastin formula [35,36] accounting for the intrinsic and extrinsic mechanisms to the spin Hall conductivity, evaluating the Fermi sea as well as the Fermi surface contributions [35] including the full vertex corrections [37]. With this fully quantum mechanical description of the charge and spin transport of the system, we are able to extract the intrinsic as well as skew-scattering contributions in the dilute limit of the alloy, which we will compare to a distinct approach based on the solution of the semiclassical Boltzmann equation [38,39].

III. RESULTS

The summary for the figure of merit, the SHA, is shown in Fig. 1 for all eight alloys in the full concentration ranges. For all fcc-based systems, the principal behavior is very similar, with low SHAs in the dilute limit and maxima for the SHA in the range $0.5 \leqslant x < 0.9$ Pt concentration. We have summarized the established maxima in Table II.

This principal behavior is generally well known and understood [40]. The dominant mechanisms for the SHE are the intrinsic [41–43] and extrinsic [3,44–48] mechanisms, with the extrinsic side jump mechanism [49,50] often playing a less important role. For the spin Hall conductivity (SHC), the extrinsic skew scattering dominates in the dilute limit [38] as the conductivity is diverging in that regime, while the intrinsic mechanism becomes dominant for concentrated alloys [35,37,40]. However, as discussed above, the SHC diverges in the dilute limit as does the longitudinal conductivity when excluding the residual resistivity. As a result, the SHA is suppressed in the dilute limit, but peaks in the concentrated regime where the suppression of the SHC is counterbalanced by the even stronger reduction of the longitudinal conductivity [40].

While this is well understood for theoretical results when structural disorder such as grain boundaries is ignored, it often fails to capture the behavior in typically polycrystalline experimental samples where the residual resistivity can be significant. For that reason, we included this contribution in a simple phenomenological model, where we considered a simple serial resistor between the theoretically evaluated longitudinal resistivity, ρ_{theo}, arising from the chemically

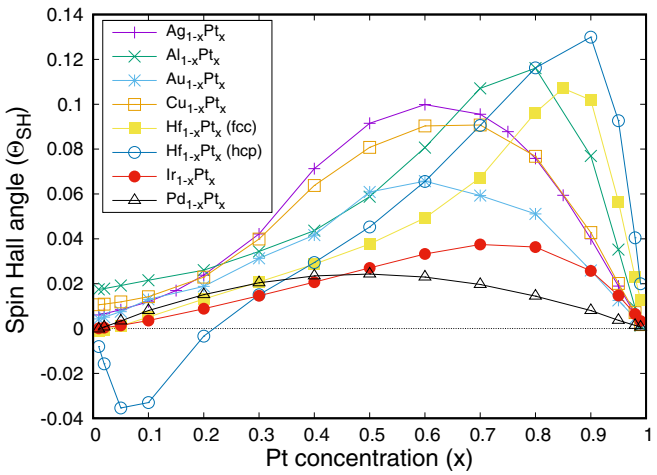

FIG. 1. Calculated spin Hall angles for all seven binary alloys across the full concentration range.

TABLE II. The maximal values for the SHAs, θ_{SH}, in all alloys $M_{1-x}Pt_x$ and the corresponding Pt concentration x, excluding (second and third columns) and including (fourth and fifth columns) the residual resistivity.

	Excl. ρ_{res}		Incl. ρ_{res}	
Material	x	θ_{SH}	x	θ_{SH}
AgPt	0.6	0.100	0.6	0.112
AlPt	0.8	0.116	0.8	0.133
AuPt	0.6	0.066	0.6	0.080
CuPt	0.7	0.091	0.7	0.106
HfPt (fcc)	0.85	0.107	0.90	0.125
HfPt (hcp)	0.9	0.130	0.90	0.148
IrPt	0.7	0.037	0.8	0.056
PdPt	0.5	0.024	0.55	0.042

disordered binary alloy and the experimentally observed residual resistivity, ρ_{res}, due to structural disorder. In this model, the total resistivity is given by

$$\rho^{\text{tot}}_{M_{1-x}Pt_x} = \rho^{\text{theo}}_{M_{1-x}Pt_x} + (1-x)\rho^{M}_{\text{res}} + x\rho^{Pt}_{\text{res}},$$

where the considered residual resistivities ρ^{M}_{res} are summarized in Table I.

The resulting curves are summarized in Fig. 2 and show a couple of marked differences to Fig. 1. First, depending on the residual resistivities, we will find the already discussed suppression of the SHAs in the dilute limit or an enhancement of the SHA as for AlPt and CuPt. The enhancement arises for cases where the residual resistivities are large in comparison to the resistivities induced by the chemical disorder in the dilute limit, i.e., weak scattering from the chemical disorder. This effect will be difficult to observe experimentally. Second, we can observe a shift in the maxima of the SHA for some of the alloys depending on the relative sizes of the residual resistivities for the distinct metallic limits. We summarized all considered residual resistivities in Table I and all SHA maxima with and without the inclusion of the residual resistivity in Table II.

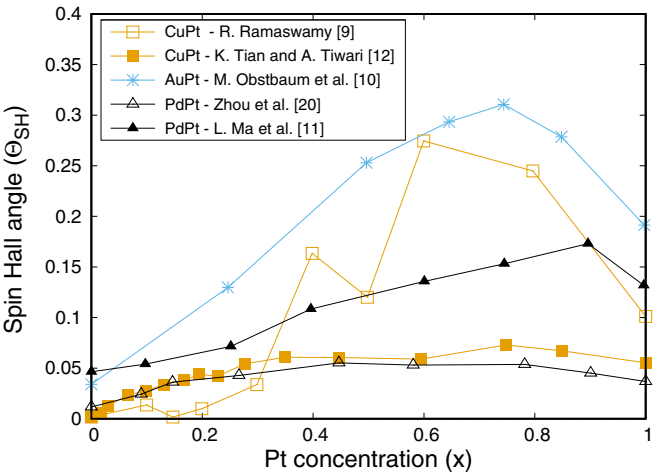

FIG. 3. Experimental spin Hall angles for $Cu_{1-x}Pt_x$ [9,12], $Au_{1-x}Pt_x$ [10], and $Pd_{1-x}Pt_x$ [11,20].

When comparing these results to the available experimental data for CuPt [9,12], AuPt [10], and PdPt [11] in the full concentration range (see Fig. 3), most trends are reasonably well reproduced. In all cases, the maximum for the SHA is above $x = 0.5$ for the Pt concentration x. However, there are also noticeable differences, namely, larger SHAs observed in experiment in contrast to theory, as well as a peak for the SHA in the PdPt alloy far into the Pt-rich region. At the same time, two very distinct SHA results have been found experimentally for the CuPt alloy [9,12], giving an indication of the reliability of the quantitative results for any given alloy.

In order to give a better microscopic insight into the above discussion, Fig. 4 shows an example for the typical behavior of the theoretically calculated SHC. Here, we show $Al_{1-x}Pt_x$, but the principal features are the same for all alloy systems. The black crosses show the total SHC including all Fermi sea and Fermi surface contributions [35,40], as well as the

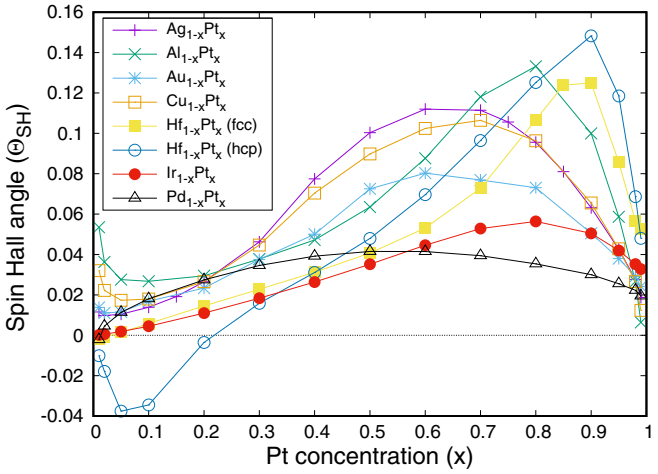

FIG. 2. Calculated spin Hall angles for all seven binary alloys across the full concentration range, including the experimentally observed residual resistivities as summarized in Table I.

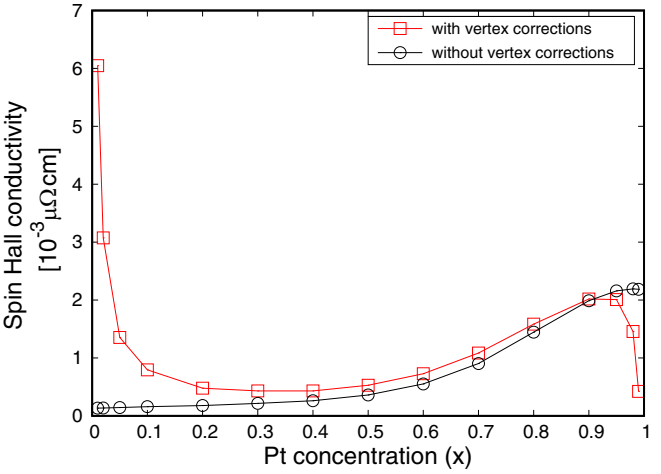

FIG. 4. Calculated spin Hall conductivities for the $Al_{1-x}Pt_x$ alloy. Results with (solid red squares) and without (solid black circles) vertex corrections are compared.

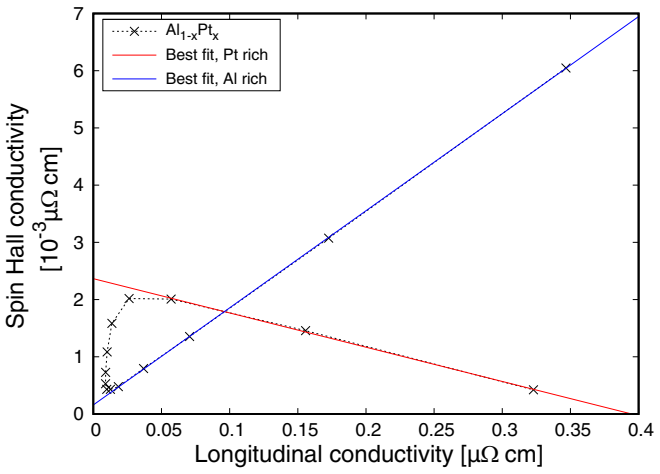

FIG. 5. The spin Hall conductivity shown as a function of the longitudinal charge conductivity for $Al_{1-x}Pt_x$. The gradient of the best fits for values in the dilute limit (solid red and dashed blue lines) defines the extrinsic spin Hall angles in these limits derived from the skew-scattering contribution.

vertex corrections. The vertex corrections account for the scattering process and are equivalent to the scattering-in term in the semiclassical Boltzmann equation in the dilute limit [37]. Comparing both, the main differences are visible for the dilute limit only, where the vertex corrections give diverging contributions when approaching the ultraclean limit. In a semiclassical picture, this clean limit corresponds to vanishing scattering and a divergence of the mean free path which scales inversely with the impurity concentration in the ultraclean limit [37,38].

Interestingly, these contributions are positive in the limit of Al(Pt), the dilute limit of Pt impurities in Al, and become negative in the limit of Pt(Al), the dilute limit of Al impurities in Pt. While this opposing behavior can often be observed for binary alloys [40,51], there is no strict rule and the actual result will depend on the detailed electronic structure of the specific alloy system. As pointed out before, the divergence of the conductivity in the clean limit equally appears for the longitudinal conductivity, thus resulting in a linear scaling between both conductivities. It is this scaling which enables us to extract the skew-scattering contributions to the SHA [37].

For the AlPt alloy, this is shown in Fig. 5, including the fits in the dilute limit, where the slope defines the skew-scattering contribution to the SHA. We extracted that parameter for all seven alloys, as shown in Table III, and compared it to the direct evaluation of the skew-scattering contribution using a solver of the Boltzmann equation [38]. Evidently, the agreement is very good, validating both methods. The only notable difference is visible for the Pt-rich $Ir_{1-x}Pt_x$ system, where the order of magnitude is in good agreement, but the sign is opposite between the two methods. However, this is an extreme example where the skew-scattering contribution is essentially vanishing as Ir introduces only very weak scattering in the Pt system. For that reason, the numerical error as well as the error in the linear fit become comparable to the actual value. The good agreement between the two methods is visually emphasized in Fig. 6, where we present the skew-scattering

TABLE III. Comparison of the skew-scattering spin Hall angles derived from the scaling relation in the dilute limit for the Kubo-Bastin transport calculations [35] and the explicit calculation within a semiclassical Boltzmann approach [38,39].

Material	Skew-scattering spin Hall angle (Kubo-Bastin)	Skew-scattering spin Hall angle (Boltzmann)
Pt(Al)	−0.0060	−0.005
Al(Pt)	0.0170	0.017
Pt(Cu)	−0.0027	−0.0025
Cu(Pt)	0.0103	0.0135
Pt(Ag)	−0.0015	−0.0015
Ag(Pt)	0.0055	0.0085
Pt(Au)	−0.0005	−0.0005
Au(Pt)	0.0035	0.005
Pt(Pd)	−0.0001	−0.0009
Pd(Pt)	−0.0012	−0.0002
Ir(Pt)	-2.00×10^{-4}	-1×10^{-4}
Pt(Ir)	1.46×10^{-4}	-6.8×10^{-5}
Pt(Hf) - fcc	0.0039	0.0035
Hf(Pt) - hcp	−0.0025	−0.0023

SHA derived from both methods in a scatter plot. Only for Cu(Pt), Ag(Pt), and Au(Pt) do we find a slightly more relevant deviation between the Kubo-Bastin- and Boltzmann-based approaches, where the Boltzmann approach appears to show consistently higher results. With this basic understanding of the microscopic processes, we aim to model the principal functional form of the spin Hall conductivity as a function of the Pt concentration x. As discussed, the four key contributions are the distinct skew-scattering contributions in the dilute limits as well as the two intrinsic contributions arising from the clean crystals, which are dominant in the dirty limit. Adding all four contributions in a parallel resistor model, we find, for the spin Hall conductivity,

$$\sigma_{SH} = \frac{a}{x} + \frac{b}{1-x} + x\sigma_{SH}^{\mathrm{intr}}(Pt) + (1-x)\sigma_{SH}^{\mathrm{intr}}(M), \qquad (2)$$

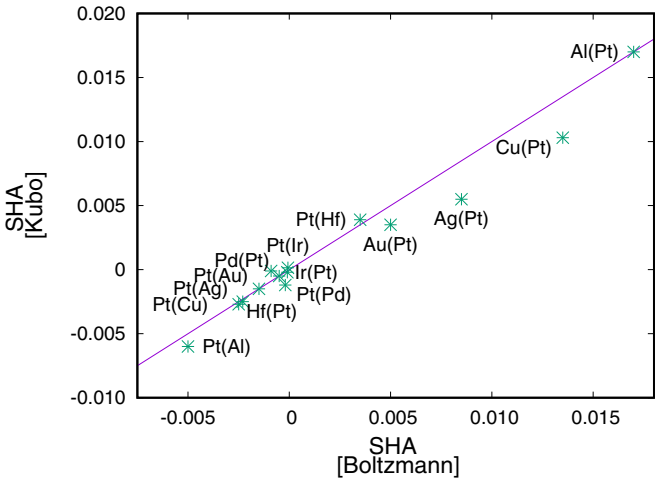

FIG. 6. Correlation between the skew-scattering spin Hall angle calculated via the Kubo formalism vs the Boltzmann formalism.

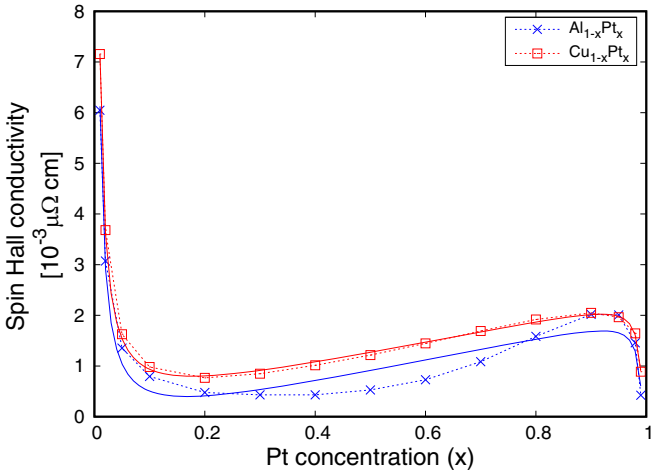

FIG. 7. Calculated spin Hall conductivity of $Al_{1-x}Pt_x$ (blue crosses) and $Cu_{1-x}Pt_x$ (red squares) in comparison to the best fit (solid lines) using the model established in Eq. (2).

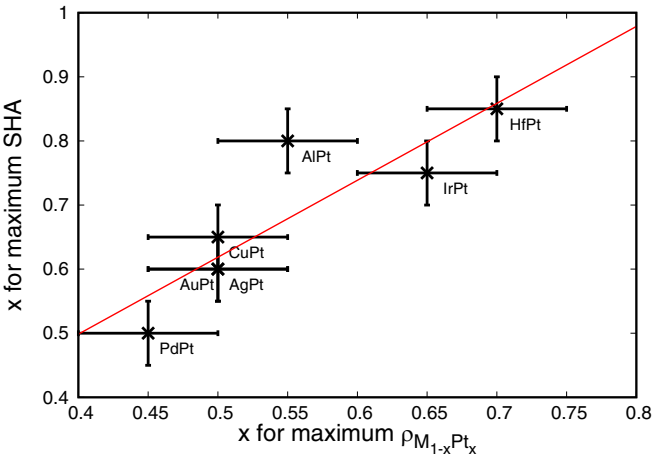

FIG. 8. Scaling between the Pt concentration at which the SHA peaks vs the Pt concentration at which the longitudinal resistivity is maximum. For cases where the SHA or the longitudinal resistivity were almost equal between the concentrations, we assumed the maximum to be at the central point in between.

where a and b represent the skew-scattering contributions from dilute alloy M(Pt) and Pt(M), respectively, and $\sigma_{SH}^{\text{intr}}(Pt)$ [$\sigma_{SH}^{\text{intr}}(M)$] is the intrinsic conductivity from the clean Pt (M) system.

In Fig. 7, we present an example for such a fit for the $Cu_{1-x}Pt_x$ as well as the $Al_{1-x}Pt_x$. Whereas the $Cu_{1-x}Pt_x$ alloy shows very good agreement between the simplified model fit to the full calculation including all different contributions, the agreement for the $Al_{1-x}Pt_x$ is slightly less perfect. With such an interpretation, the SHC in the full concentration is reduced to only four parameters. Similarly, the longitudinal charge conductivity can be modeled via

$$\sigma^{\text{theo}}_{M_{1-x}Pt_x} = \frac{\sigma_{Pt}}{x} + \frac{\sigma_M}{1-x}, \tag{3}$$

which enables us to define the skew-scattering Hall angles as

$$\theta_{sk}(Pt) = \frac{a}{\sigma_{Pt}} \text{ and } \theta_{sk}(M) = \frac{b}{\sigma_M}, \tag{4}$$

respectively. Initially, it might seem appealing to use these model equations to make simple predictions for the optimization of the maxima in the SHA as they contain only six often readily available parameters. While these equations are sufficient to describe the calculated functional form, they are unfortunately rather complicated when trying to predict the size and the position of the maxima as a function of the Pt concentration.

Due to the difficulty of predicting the peak of the SHA within this model, we aim to simplify the model to predict the concentration position at which the maximum value of the SHA occurs in binary Pt-based alloys. First, to simplify the problem, the residual resistivity may be neglected. In this case, the maximum of the SHA is slightly reduced, but the overall functional form of the SHA dependence on the Pt concentration remains unaltered. As the calculated SHA peaks lie within the concentrated regimes for the binary alloys, a further simplification of Eq. (2) is to neglect the skew scattering in the relevant region,

$$\sigma_{SH} = x\sigma_{SH}^{\text{intr}}(Pt) + (1-x)\sigma_{SH}^{\text{intr}}(M). \tag{5}$$

Equation (5) models the SHC as linearly increasing between the intrinsic M value and the intrinsic Pt value as a function of alloy concentration. This is a poor fit to the calculated data for the SHC in the dilute regions, but a decent fit for the concentrated alloy, which is the region of concern. Within this further approximation, the position of the SHA is determined by the peaks in longitudinal resistivity. The relationship between the concentration at which the peaks in longitudinal resistivity occur compared to the position of the peak of SHA is tested in Fig. 8. For almost all systems, the scaling works well apart from AlPt, which deviates from the overall trend already indicated by the difficulties in fitting the SHC, as shown in Fig. 7.

In order to further explore what is causing the scaling of the peak for the SHA with the peak in resistivity, let us consider that the SHC is assumed to be linear in Eq. (5). This implies that the only free parameter in the SHC changing between systems is the intrinsic SHC of the second element M, $\sigma_{SH}^{\text{intr}}(M)$. This parameter determines the gradient of the linear approximation to SHC. Therefore, even though the peak in the SHA is caused by the longitudinal resistivity, it is shifted by $\sigma_{SH}^{\text{intr}}(M)$, which makes it the most important parameter in predicting the position of that peak, as shown in Fig. 9. For elements with an intrinsic SHC comparable to Pt, such as Pd, the alloy system will have peaks that are centered around the 50% alloy position. In contrast, for those with wildly deviating intrinsic spin Hall conductivities, such as Hf which has a negative intrinsic spin Hall conductivity, the SHA peaks at higher concentrations.

Although the intrinsic spin Hall conductivity of element M is a good indicator of where the SHA will peak for binary Pt-based alloys, it is not useful as an indicator of how large the SHA will be at its maximum. The parameter that is the best indicator for the size of the SHA is the size of the longitudinal resistivity at the maximum for the alloy. Figure 10 shows that for five of the seven systems that are investigated, the value of the longitudinal resistivity at the maximum is a near perfect indicator for the maximum SHA. However, there are

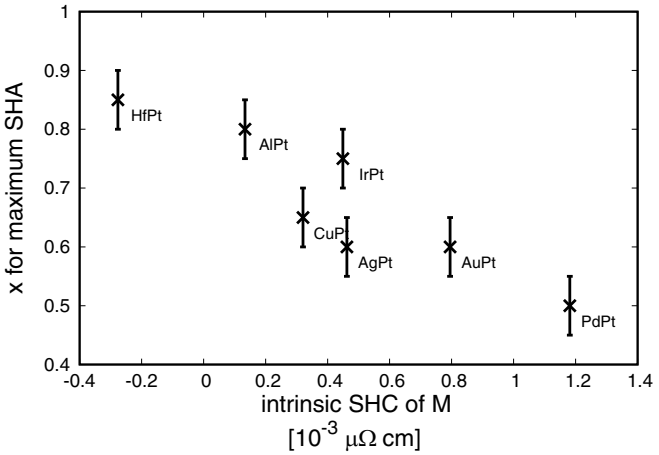

FIG. 9. Pt concentration for the spin Hall angle maximum as a function of the intrinsic spin Hall conductivity for element M in the binary alloy $M_{1-x}Pt_x$. For cases where the SHA maximum was approximately equivalent between two concentrations, we assumed the maximum to be at the average concentration.

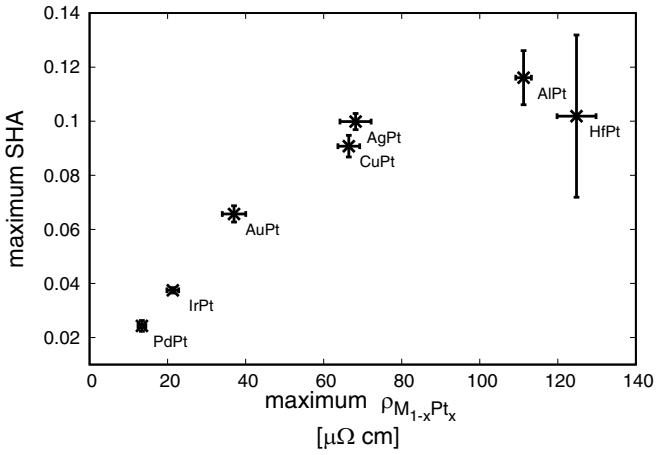

FIG. 10. Maximum value of spin Hall angles vs the maximum of the longitudinal resistivity for binary Pt-based alloys $M_{1-x}Pt_x$.

exceptions in AlPt and HfPt. For these two systems, Eq. (5) is less applicable and a linear fit in the concentrated regime is far from perfect. This is due to these systems having partner elements that are very different from that of Pt, whereas the other five are much closer in terms of atomic structure. Still, even for those two systems, the maximum longitudinal resistivity being large is a good indicator that the maximum spin Hall angle will be too.

IV. CONCLUSIONS

In this work, we have used multiple first-principles KKR-based approaches to calculate the full spin Hall conductivity (intrinsic and skew scattering), longitudinal conductivity, and spin Hall angle for several different Pt-based, chemically disordered binary alloys. When including the experimental residual resistivities, the maximum spin Hall angle that we identified is 13% in $Al_{0.2}Pt_{0.8}$ and $Hf_{0.1}Pt_{0.9}$, which is comparable to the best spin Hall angles experimentally found in good metal systems. The spin Hall conductivity and longitudinal conductivity for these alloys can be fit using two equations and six parameters. However, an analytical expression for the concentration for the maximum spin Hall angle is not suitable for practical calculations. We find that the high intrinsic spin Hall conductivity observed in Pt is fairly robust to alloying for Pt concentrations greater than 60%. The concentration where the maximum spin Hall angle occurs is linearly dependent on the difference in spin Hall conductivity between Pt and the alloying element M. For elements such as Pd with spin Hall conductivity close to Pt, the spin Hall angle peaks near 50% Pt. For alloying elements with spin Hall conductivity drastically different from Pt, the spin Hall angle maximum occurs at high Pt concentrations. Our calculations also indicate, for many alloys, that the maximum of the longitudinal resistivity is a good predictor of the maximum spin Hall angle for that alloy. The trends identified in this broad study of Pt-based alloys should aid in experimental efforts to optimize Pt-based materials for spin-orbit torque applications.

ACKNOWLEDGMENTS

The work in this paper was carried out using the computational facilities of the Advanced Computing Research Centre, University of Bristol [52]. O.M. gratefully acknowledges scholarship support through the EPSRC funded Centre for Doctoral Training in Condensed Matter Physics (Grant No. EP/L015544/1) and the Western Digital academic program.

[1] M. I. Dyakonov and V. I. Perel, Sov. Phys. JETP Lett. **13**, 467 (1971).
[2] M. Dyakonov and A. Khaetskii, *Spin Physics in Semiconductors*, 2nd ed. (Springer, Berlin, 2017).
[3] J. Sinova, S. O. Valenzuela, J. Wunderlich, C. H. Back, and T. Jungwirth, Rev. Mod. Phys. **87**, 1213 (2015).
[4] M. I. Dyakonov, Spin Hall effect, in *Spintronics*, edited by M. Razeghi, H.-J. M. Drouhin, and J.-E. Wegrowe (SPIE, 2008).
[5] R. Zand, A. Roohi, and R. F. DeMara, IEEE Trans. Very Large Scale Integrat. (VLSI) Syst. **25**, 2394 (2017).
[6] L. Liu, R. A. Buhrman, and D. C. Ralph, arXiv:1111.3702.
[7] G.-Y. Guo, S. Murakami, T.-W. Chen, and N. Nagaosa, Phys. Rev. Lett. **100**, 096401 (2008).
[8] M.-H. Nguyen, D. C. Ralph, and R. A. Buhrman, Phys. Rev. Lett. **116**, 126601 (2016).
[9] R. Ramaswamy, Y. Wang, M. Elyasi, M. Motapothula, T. Venkatesan, X. Qiu, and H. Yang, Phys. Rev. Appl. **8**, 024034 (2017).
[10] M. Obstbaum, M. Decker, A. K. Greitner, M. Haertinger, T. N. G. Meier, M. Kronseder, K. Chadova, S. Wimmer, D. Ködderitzsch, H. Ebert *et al.*, Phys. Rev. Lett. **117**, 167204 (2016).

[11] L. Ma, L. Lang, J. Kim, Z. Yuan, R. Wu, S. Zhou, and X. Qiu, Phys. Rev. B **98**, 224424 (2018).
[12] K. Tian and A. Tiwari, Sci. Rep. **9**, 3133 (2019).
[13] L. Zhu, D. C. Ralph, and R. A. Buhrman, Phys. Rev. Appl. **10**, 031001 (2018).
[14] L. Zhu, L. Zhu, S. Shi, D. C. Ralph, and R. A. Buhrman, Adv. Electron. Mater. **6**, 1901131 (2020).
[15] Y. Xu, Y. Yang, H. Xie, and Y. Wu, Appl. Phys. Lett. **115**, 182406 (2019).
[16] Y. Saito, N. Tezuka, S. Ikeda, H. Sato, and T. Endoh, AIP Adv. **9**, 125312 (2019).
[17] A. Hrabec, K. Shahbazi, T. A. Moore, E. Martinez, and C. H. Marrows, Nanotechnology **30**, 234003 (2019).
[18] Y. Ou, D. C. Ralph, and R. A. Buhrman, Phys. Rev. Lett. **120**, 097203 (2018).
[19] M.-H. Nguyen, S. Shi, G. E. Rowlands, S. V. Aradhya, C. L. Jermain, D. Ralph, and R. Buhrman, Appl. Phys. Lett. **112**, 062404 (2018).
[20] X. Zhou, M. Tang, X. L. Fan, X. P. Qiu, and S. M. Zhou, Phys. Rev. B **94**, 144427 (2016).
[21] L. Zhu, K. Sobotkiewich, X. Ma, X. Li, D. C. Ralph, and R. A. Buhrman, Adv. Funct. Mater. **29**, 1805822 (2019).
[22] S. O. Valenzuela and M. Tunkham, Nature (London) **442**, 176 (2006).
[23] J. W. C. De Vries, Thin Solid Films **167**, 25 (1988).
[24] G. Mihajlović, J. E. Pearson, M. A. Garcia, S. D. Bader, and A. Hoffmann, Phys. Rev. Lett. **103**, 166601 (2009).
[25] F. J. Jedema, A. T. Filip, and B. J. Van Wees, Nature (London) **410**, 345 (2001).
[26] F. W. Clinard and C. P. Kempter, J. Less-Common Met. **15**, 59 (1968).
[27] E. Selbach, H. Jacques, K. Eiermann, B. Lengeler, and W. Schilling, Thin Solid Films **149**, 17 (1987).
[28] L. Vila, T. Kimura, and Y. C. Otani, Phys. Rev. Lett. **99**, 226604 (2007).
[29] H. Ebert, D. Ködderitzsch, and J. Minár, Rep. Prog. Phys. **74**, 096501 (2011).
[30] P. Soven, Phys. Rev. **156**, 809 (1967).
[31] W. H. Butler, Phys. Rev. B **31**, 3260 (1985).
[32] H. Akai, J. Phys.: Condens. Matter **1**, 8045 (1989).
[33] J. K. Stalick and R. M. Waterstrat, J. Phase Equilib. Diffus. **35**, 15 (2014).
[34] S. H. Vosko, L. Wilk, and M. Nusair, Can. J. Phys. **58**, 1200 (1980).
[35] D. Ködderitzsch, K. Chadova, and H. Ebert, Phys. Rev. B **92**, 184415 (2015).
[36] A. Bastin, C. Lewiner, O. Betbeder-Matibet, and P. Nozieres, J. Phys. Chem. Solids **32**, 1811 (1971).
[37] S. Lowitzer, M. Gradhand, D. Ködderitzsch, D. V. Fedorov, I. Mertig, and H. Ebert, Phys. Rev. Lett. **106**, 056601 (2011).
[38] M. Gradhand, D. V. Fedorov, P. Zahn, and I. Mertig, Phys. Rev. Lett. **104**, 186403 (2010).
[39] M. Gradhand, D. V. Fedorov, P. Zahn, and I. Mertig, Phys. Rev. B **81**, 245109 (2010).
[40] I. Turek, J. Kudrnovský, and V. Drchal, Phys. Rev. B **100**, 134435 (2019).
[41] R. Karplus and J. M. Luttinger, Phys. Rev. **95**, 1154 (1954).
[42] J. Sinova, D. Culcer, Q. Niu, N. A. Sinitsyn, T. Jungwirth, and A. H. MacDonald, Phys. Rev. Lett. **92**, 126603 (2004).
[43] M. Gradhand, D. V. Fedorov, F. Pientka, P. Zahn, I. Mertig, and B. L. Györffy, J. Phys.: Condens. Matter **24**, 213202 (2012).
[44] N. F. Mott and H. S. Massey, *The Theory of Atomic Collisions* (Clarendon, Oxford, 1965).
[45] M. I. Dyakonov and V. I. Perel, Phys. Lett. A **35**, 459 (1971).
[46] J. Smit, Physica **21**, 877 (1955).
[47] J. Smit, Physica **24**, 39 (1958).
[48] Y. Niimi, Y. Kawanishi, D. H. Wei, C. Deranlot, H. X. Yang, M. Chshiev, T. Valet, A. Fert, and Y. Otani, Phys. Rev. Lett. **109**, 156602 (2012).
[49] L. Berger, Phys. Rev. B **2**, 4559 (1970).
[50] L. Berger, Phys. Rev. B **5**, 1862 (1972).
[51] M. Gradhand, D. V. Fedorov, P. Zahn, I. Mertig, Y. Otani, Y. Niimi, L. Vila, and A. Fert, SPIN **02**, 1250010 (2012).
[52] http://www.bris.ac.uk/acrc/.